Plasma Phys. Control. Fusion **54** (2012) 065010 (8pp) doi:10.1088/0741-3335/54/6/065010

Impurity analysis of NSTX using a transmission grating-based imaging spectrometer

Deepak Kumar[1], Michael Finkenthal[1], Dan Stutman[1], Ronald E Bell[2], Daniel J Clayton[1], Ahmed Diallo[2], Ben P LeBlanc[2], Mario Podesta[2] and Kevin Tritz[1]

[1] Department of Physics and Astronomy, The Johns Hopkins University, Baltimore, MD 21218, USA
[2] Princeton Plasma Physics Laboratory, Princeton University, Princeton, NJ 08543, USA

E-mail: deepak@pha.jhu.edu

Received 29 November 2011, in final form 20 April 2012
Published 23 May 2012
Online at stacks.iop.org/PPCF/54/065010

Abstract
A transmission grating-based imaging spectrometer has recently been installed and operated on the National Spherical Torus Experiment (NSTX) at PPPL. This paper describes the spectral and spatial characteristics of impurity emission under different operating conditions of the experiment—neutral beam heated, ohmic heated and RF heated plasma. A typical spectrum from each scenario is analyzed to provide quantitative estimates of impurity fractions in the plasma.

(Some figures may appear in colour only in the online journal)

1. Introduction

Monitoring and eventually preventing the loss of power by radiation from impurities in magnetic fusion experiments is an important part of fusion physics research. A wide variety of impurities ranging from low Z elements such as Li, C, O to high Z elements such as Fe, Mo, W have been observed in tokamak plasmas [1]. Spectroscopy in the XUV range has the benefit of being able to monitor radiation from the ground state of many impurity ion charge states and is useful in studying edge impurity behavior and impurity transport. For example, recently a space resolved XUV spectrometer was used to study the impurity transport and ergodic magnetic field structure on LHD [2].

A transmission grating-based imaging spectrometer (TGIS) [3, 4] was designed and built by the plasma spectroscopy group at the Johns Hopkins University. The spectrometer operated on the National Spherical Torus Experiment (NSTX). The spectrometer operates in a survey mode with a wavelength coverage from 30 to 700 Å, and a resolution of $\delta\lambda/\lambda \sim 3\%$. The 22° field of view of the spectrometer measures emission between 0.9 m $< R <$ 1.5 m, with a spatial resolution of 2.7 cm. The time resolution of the spectrometer was limited in the experiments described in this paper by the image readout speed of ∼400 ms. An upgraded version of the spectrometer with an order of magnitude better time resolution has been tested on a low temperature reflex discharge [4]. The design of the instrument and calibration of the grating have been described in earlier publications [3, 4]. This paper describes measurements of space localized emissivities of spectra originating from charge-exchange and electron excited emission in NSTX plasmas.

The paper is organized as follows: section 2 describes the operating principle of the transmission grating-based spectrometer. This section also describes the process of absolute calibration of the spectrometer and the expected variation of efficiency over the wavelength range covered by the spectrometer. Three prominent plasma heating mechanisms are employed on NSTX—neutral beam, ohmic and radio frequency. The spectra obtained from these heating scenarios are described in section 3. Discussion of the spectra and derivation of quantitative impurity fractions in the plasma is covered in section 4. Section 5 concludes the paper with a discussion of applications and upgrades of the spectrometer.

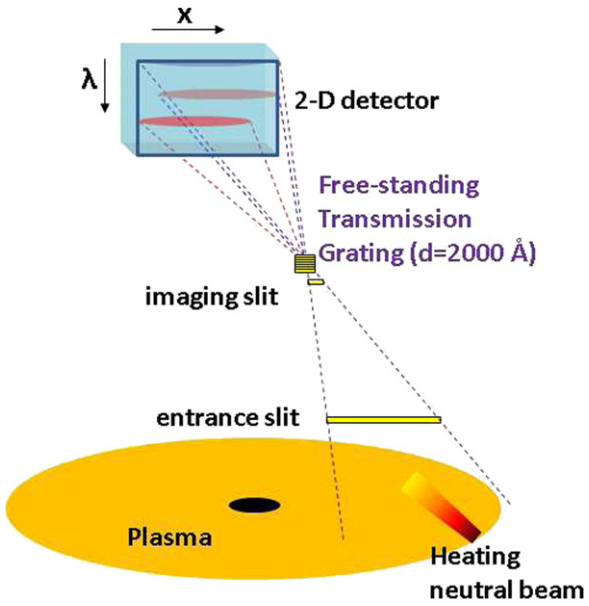

Figure 1. The TGIS spectrometer is shown imaging the mid-plane of NSTX with the heating neutral beam within its field of view.

2. The spectrometer

Figure 1 shows the working principle of the TGIS: the entrance and the imaging slit limit the view of the spectrometer along the horizontal mid-plane of NSTX. The width of the imaging slit provides the spatial resolution of the spectrometer. The wavelength dispersion is provided by a free standing transmission grating, and thus the measured spectrum on the 2D detector has both the wavelength and spatial resolution. For the data presented in this paper, a CsI coated micro-channel plate (MCP) was used as the 2D detector. The wavelength resolution of the spectrometer is determined by the number of grating periods within the slit height and the angle subtended by the height of imaging slit on the detector [5].

Figure 2(*a*) shows the mid-plane section of NSTX showing the density distribution of neutrals from the heating neutral beams and the view of the TGIS with respect to it. NSTX is a low aspect ratio ($R/a \geqslant 1.26$) spherical tokamak where the last closed flux surface (LCFS) is typically at a radius of ∼1.4–1.5 m and the magnetic axis at about 1 m. Thus the TGIS measures space-resolved XUV impurity emission from both charge exchange of low and medium Z impurities with heating neutral beams and collisionally excited emission from the edge/pedestal and from the core during ramp down and radiative collapse. During the 2010 run of NSTX the region with tangency radius $R_T < 1.1$ m was vignetted because of a misalignment of slits within the TGIS. The figures in this paper show the spectrum from the vignetted spatial region, even though no quantitative results are derived from this region.

2.1. Absolute photometric calibration of TGIS

To obtain an absolute photometric calibration of TGIS, the brightness of the C VI $n = 3$–2 charge-exchange line was simulated for NSTX conditions and compared with the brightness measured by the TGIS. The calibration is described below.

The three heating neutral beams on NSTX inject deuterium neutrals and operate at typical accelerating voltage of $V = 90$ kV. Because of the presence of molecular residuals in the neutral beam source, the neutrals emerge at energies $E_j = V/j$, where $j = 1, 2, 3$. The divergence of the neutral beam and the fractional abundance of neutrals at various energies has been calibrated for the different beams [6]. The beam is collisionally attenuated inside the plasma; thus, the relative decrease in neutral beam density is given by $-\frac{\mathrm{d}I}{I(x)} = \sigma(\boldsymbol{x}) n_\mathrm{e}(x) \mathrm{d}l$, where d$l$ is the incremental linear path length of the beam neutrals and σ is the beam stopping cross section. σ depends on the energy of the neutrals, the electron density, temperature and the impurity concentrations. For this paper, the beam stopping cross section was calculated using coefficients similar to those described by Janev *et al* [7]. An illustration of the calculated neutral beam density for a particular energy of beam atoms is shown in figure 2(*a*).

The absolutely calibrated charge-exchange spectroscopy system (CHERS) on NSTX measures the emission from C VI $n = 8$–7 line [8], and is used to calculate the mid-plane spatial density of fully stripped carbon, $n(\mathrm{C}^{6+})$. The NSTX mid-plane emissivity from the C VI $n = 3$–2 charge-exchange line can thus be calculated as

$$\epsilon_{3-2}(\boldsymbol{x}) = \sum_{\text{beams}} \sum_{j=1}^{3} n(\mathrm{C}^{6+}) v_j n_{n,j}(\boldsymbol{x}) \sigma_{3-2}(v_j), \qquad (1)$$

where v_j is the velocity of the neutral beam particles with energy E_j, $n_{n,j}$ is the density of those neutral particles, and σ_{3-2} is the charge-exchange emission cross section for the transition. Unless otherwise mentioned, the charge-exchange emission cross sections were obtained from Isler [9]. Figure 2(*b*) shows an example of the mid-plane emissivity of C VI $n = 3$–2 charge-exchange line.

The brightness measured by the TGIS along a line of sight (parameterized by the viewing angle θ) is

$$L_{3-2}(\theta) = \frac{1}{4\pi} \int\int \epsilon_{3-2}(\boldsymbol{x})\, \mathrm{d}l\, \mathrm{d}t, \qquad (2)$$

where the length integral is along the line of sight and the time integral over the exposure time of the spectrum. The measured brightness of the charge exchange line is compared with the simulated brightness in figure 3. The scaling factor for the measured line profile provides the absolute calibration for the TGIS. As seen from figure 3, the measured and simulated brightness profiles match fairly well. The better match from the measured profile of the second order radiation can be attributed to the slight saturation in the detector for the signal measured at 182 Å.

The calibration process described above did not account for three other sources of line emission C VI $n = 3$–2. These are (a) Electron excited emission in the edge from the collisions between electrons and C^{5+}, (b) charge exchange between halo neutrals from the neutral beams and fully stripped carbon ions, and (*c*) charge-exchange between the wall recycled neutrals and fully stripped carbon ions. The contribution

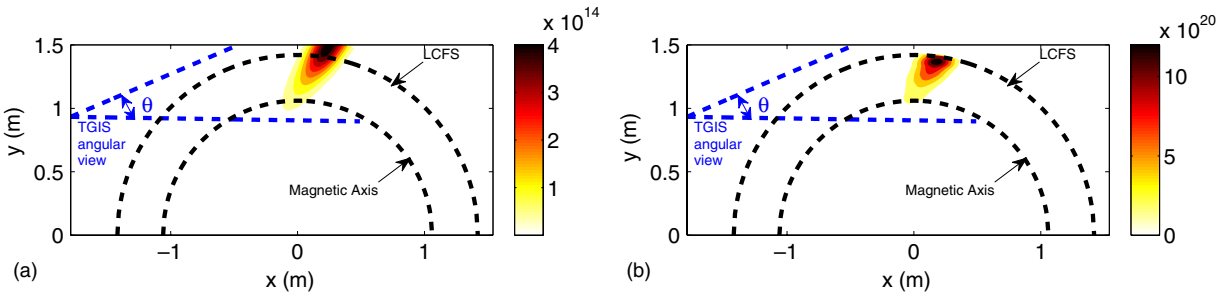

Figure 2. Mid-plane view of the TGIS on NSTX showing the magnetic axis and the LCFS. (*a*) The color contours represent the neutral density (m^{-3}) from heating neutral beams at an energy of 90 kV, at $t = 0.7$ s, shot # 142192. (*b*) The color contours represent the emissivity from charge-exchange C VI (3–2) in photons m^{-3} s^{-1}, at $t = 0.7$ s, shot # 142192.

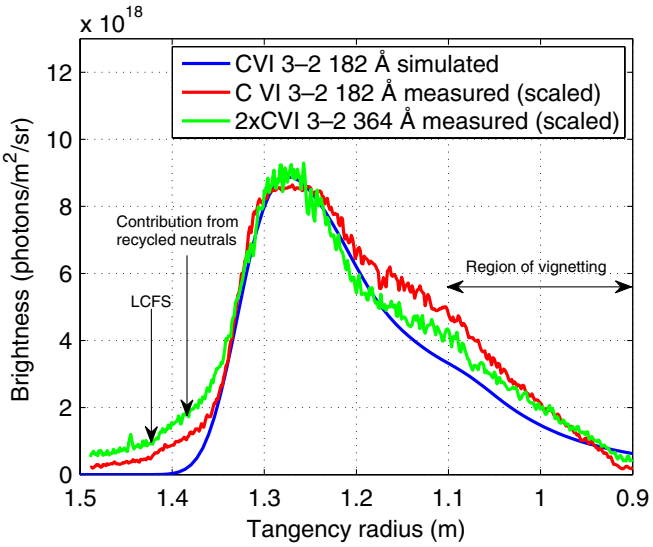

Figure 3. Comparison between measured and simulated brightness of charge-exchange C VI $n = 3$–2 line (see experimental spectrum in figure 6).

from these three effects may be a significant fraction of the measured charge-exchange brightness [10] and so their relative contributions are described next. For the typical NSTX parameters (n_e, T_e), the brightness of the collisionally excited C VI $n = 3$–2 radiation is two orders of magnitude lower than the brightness of the charge exchange from the heating neutral beam. Thus neglecting the contribution from electron excited emission does not introduce significant errors in the calibration process above. The density of the halo neutrals was simulated by the FIDASIM code [11] and was found to be higher than the density of active beam neutrals. However, their contribution to the measured charge-exchange brightness by the TGIS is on the order of $\lesssim\sqrt{T_i/E_j}$ of the active charge-exchange signal and is again negligible. In contrast, the contribution from the charge-exchange signal from the recycled wall neutrals can be significant if the recycled neutral density is high. Figure 3 shows the location of LCFS and also an arrow pointing to the contribution of charge exchange from the recycled neutrals. The contribution of these recycled wall neutrals is expected to peak in the edge near the LCFS and not where the peak in active charge-exchange brightness is measured. Thus, neglecting the effect of recycled neutrals underestimates the calibration factor derived above by as much as 15%.

2.2. *Efficiency of the TGIS over the wavelength range*

The diffraction efficiency of the grating is fairly uniform (∼10%) in the wavelength range 100–300 Å [3], and the efficiency of the CsI coated MCP detector is expected to vary within a factor of 2 in the wavelength range 100–440 Å [12]. The measured and simulated brightness of the C VI $n = 4$–3 line at 521 Å were compared with each other similar to figure 3. It was found that the efficiency of the TGIS (grating and detector combined) falls by 42%. Because of this decrease in the efficiency with increasing wavelength, the quantitative estimates of Cl and Fe concentration given in section 4 are underestimates. These concentrations were determined by observing transitions at 384 Å and 335 Å, respectively (see figure 6).

This section described the absolute photometric and the relative wavelength calibration of the TGIS from data gathered on NSTX. However, calibration on a synchrotron radiation facility is expected to be more accurate and is being planned.

3. Results

3.1. *Spectra obtained from ohmic plasmas*

Carbon, lithium and oxygen were the typical impurities detected in NSTX ohmic plasmas. Spectrum obtained from the L-mode ohmic shot # 141739 is shown in figure 4. The most prominent emitting ions in this spectrum are Li III, C IV and C VI. As one can see, the emission from C IV is localized to the outermost edges of the plasma $R \sim 1.4$ m, while Li III and C VI are emitting further inward. The localized emissivities are presented in detail in section 4.1. The typical core electron density and temperature during the current flat top were $n_e \sim 3 \times 10^{13}$ cm^{-3} and $T_e \sim 0.6$ keV. The plasma parameters for this shot are described in figure 5. The exposure time for the TGIS detector is more than the typical duration of ohmic plasmas, and so the spectrum covers the ramp down as well (see figure 5(*a*)).

3.2. *Spectra obtained from neutral beam heated plasmas*

Figure 6 shows a typical spectrum obtained from a neutral beam heated H-mode plasma shot # 142192 on NSTX. The typical core electron densities and temperature during this time were

$n_e \sim 8 \times 10^{13}\,\mathrm{cm}^{-3}$ and $T_e \sim 0.9\,\mathrm{keV}$, respectively. The plasma parameters for this shot are shown in figure 7. The dotted red lines in the spectrum show the region of intense beam interaction ($1.32\,\mathrm{m} > R_T > 1.21\,\mathrm{m}$), where the density of beam neutrals is high (see figure 2). The spectrum in this spatial region is dominated by charge exchange from low Z impurities such as C and O. Emission from medium Z impurities such as Cl and Fe consists of both the charge-exchange and electron excited emission from the edge.

A 'spectral cut' at tangency radius $R_T = 1.27\,\mathrm{m}$ is shown in figure 8. The red arrow in the figure indicates that the spectrum from NB plasma has a significant continuum contribution at wavelengths below 300 Å. This continuum is from Bremsstrahlung and higher order diffraction of radiation, primarily from carbon charge exchange. The quantitative estimates made in the next section are carried out by empirically subtracting the continuum contribution from the measured spatial profiles of the spectral lines.

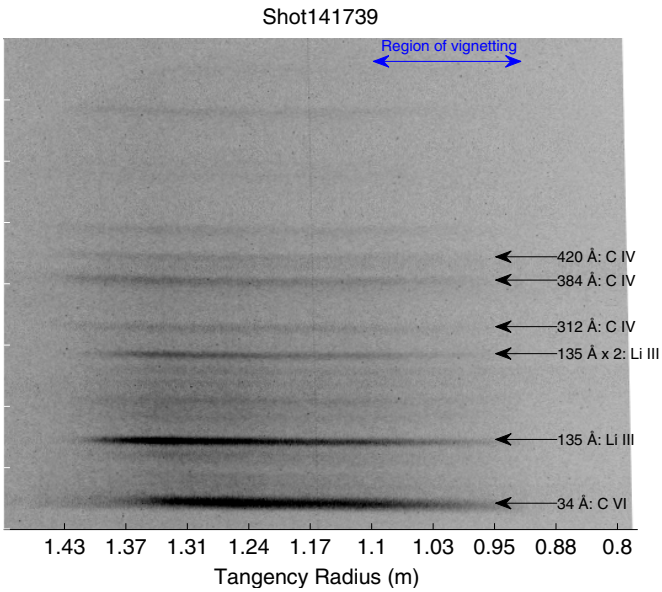

Figure 4. Example of a TGIS spectrum from an L-mode ohmic NSTX plasma.

3.3. Spectra obtained from RF heated plasmas

In the NSTX tokamak, auxiliary heating by RF antennas was provided either for deuterium plasmas or for helium plasmas. Figure 9(*a*) shows a spectrum obtained from RF heated deuterium plasma (shot #142001). The typical core electron density and temperature for this shot were $n_e \sim 3 \times 10^{13}\,\mathrm{cm}^{-3}$ and $T_e \sim 0.8\,\mathrm{keV}$. Figure 9(*b*) shows a spectrum obtained from RF heated helium plasma (shot #141857). The typical core electron density and temperature in this case were $n_e \sim 2 \times 10^{13}\,\mathrm{cm}^{-3}$ and $T_e \sim 1.2\,\mathrm{keV}$. Similar to the ohmic shots, the exposure time of the spectrum from RF shot includes the period of ramp down as well.

The TGIS detects emission from Na-like Cu in figure 9(*a*) as Cu is introduced into the plasma from arcing in the RF antenna. The brightness of the Na-like Cu in figure 9(*a*) peaks in the mid-radius region at $R \sim 1.3\,\mathrm{m}$ and not in the c ore, which is consistent with coronal equilibrium charge state distribution of Cu [13].

In the He plasma (see figure 9(*b*)), the most prominent impurity is Li. The local emissivity of He II and Li III also peaks in the edge, exhibiting a very wide spatial profile. The He and Li concentrations calculated from their peak emissivities are $n(\mathrm{He}^{1+}) \sim 1.5 \times 10^{-3} \times n_e$ and $n(\mathrm{Li}^{2+}) \sim 10^{-3} \times n_e$. The procedure for deriving these impurity fractions is described in section 4.1.

4. Discussion

4.1. Localized emissivity from ohmic heated NSTX plasmas

The spectrum from ohmic heated plasma, presented in section 3.1, is analyzed further in this section to determine the impurity fractions and show the space localized emissivities

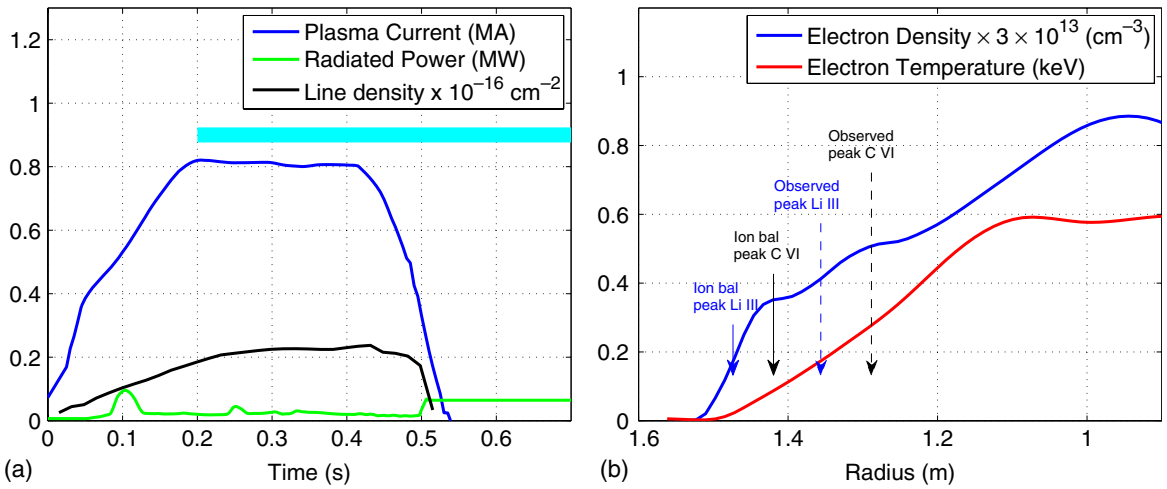

Figure 5. Plasma parameters for the spectrum shown in figure 4. (*a*) Plasma toroidal current, radiated power and line-averaged electron density as a function of time. The cyan rectangle shows the exposure time of the spectrum. (*b*) Mid-plane electron density and temperature averaged over $0.2 < t < 0.4\,\mathrm{s}$. The solid arrows denote the expected location of peak Li III and C VI emissivity based on equilibrium ionization balance (no transport). The dotted arrows denote the location of maximum Li III and C VI emissivity measured by the TGIS (see figure 10(*b*)).

from the impurities. The brightness from Ly-α emission from Li, C and 2p–3d transition from C IV are shown in figure 10(a). The corresponding Abel inverted emissivity profiles are shown in figure 10(b). The spatially localized emissivity profiles thus obtained highlight the capability of the TGIS to do space-resolved measurements. In the absence of transport, the Li and C emissivities should have peaked at radii 1.47 m and 1.43 m, respectively. However, the significant inward shift in their peak emissivity (see figure 10(b)) can be caused by transport and change in ionization equilibrium through recombination from thermal neutrals [14]. Figure 10(b) shows a second peak in the emissivity of Ly-α radiation from C. The origin of this second peak is currently unknown.

As seen from figure 5(a), the exposure time of the spectrum covers the ramp down. The contribution from the ramp down may have caused the wide emissivity profiles and the second bump in the C emissivity at a radius of 1.17 m shown in figure 10(b).

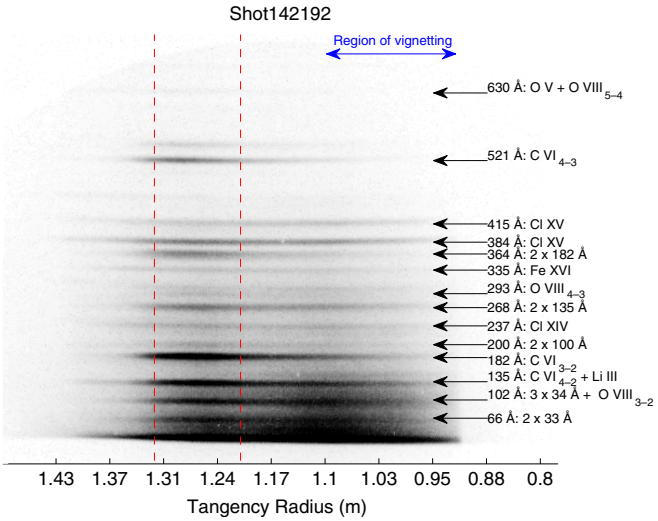

Figure 6. Spectrum from a typical neutral beam heated NSTX plasma. The principal quantum numbers of the charge-exchange transitions are shown in subscript.

The localized emissivities shown in figure 10(b) can be used to calculate the impurity density. Assuming

$$\text{Emissivity}(x_0) = \int \epsilon(n_e, T_e) \times f \times n_e(x_0) \times n_e(x_0) \mathrm{d}t, \quad (3)$$

where ϵ is the photon emissivity coefficient for electron excited emission derived from the ADAS atomic database [15], f is the impurity fraction of a particular charge state, and x_0 is the radial location of the peak emissivity (for example, $x_0 = 1.37$ m for Li III in figure 10(b)). The time integral is performed for the exposure time of the spectrum, during which the plasma current is constant. Equation (3) can be used to estimate the impurity fraction, f, if it is assumed to be constant in time. Thus, the peak impurity fractions from figure 10(b) are $n(C^{3+}) \sim 4 \times 10^{-5} \times n_e$, $n(C^{5+}) \sim 2 \times 10^{-3} \times n_e$ and $n(Li^{2+}) \sim 3 \times 10^{-4} \times n_e$.

4.2. Impurity fractions in neutral beam heated NSTX plasmas

The spectrum from neutral beam heated plasma shows that carbon is the most prominent low Z impurity in neutral beam heated experiments (see figure 6). The impurity fraction of carbon is usually of the order of $\sim 0.05 \times n_e$, as measured by an optical charge-exchange system [8]. By simulating the brightness of the charge-exchange signal from O VIII $n = 4$–3 transition, it was found that the fraction of fully stripped oxygen was of the order of $\sim 0.002 \times n_e$ at the peak of the beam interaction region.

Introduction of lithium at the edge of various fusion experiments has shown favorable increase in fusion power [16] and in energy confinement times [16, 17]. NSTX is investigating the effect of lithium wall coatings by evaporating lithium onto the walls and a heated lower divertor plate. A significant result from the NSTX experiments was the evidence that even with extensive Li conditioning of the carbon walls, the lithium does not contaminate the plasma [18–20]. In fact, the optical charge-exchange system found the concentration of fully stripped Li inside the plasma to be 2 orders of magnitude

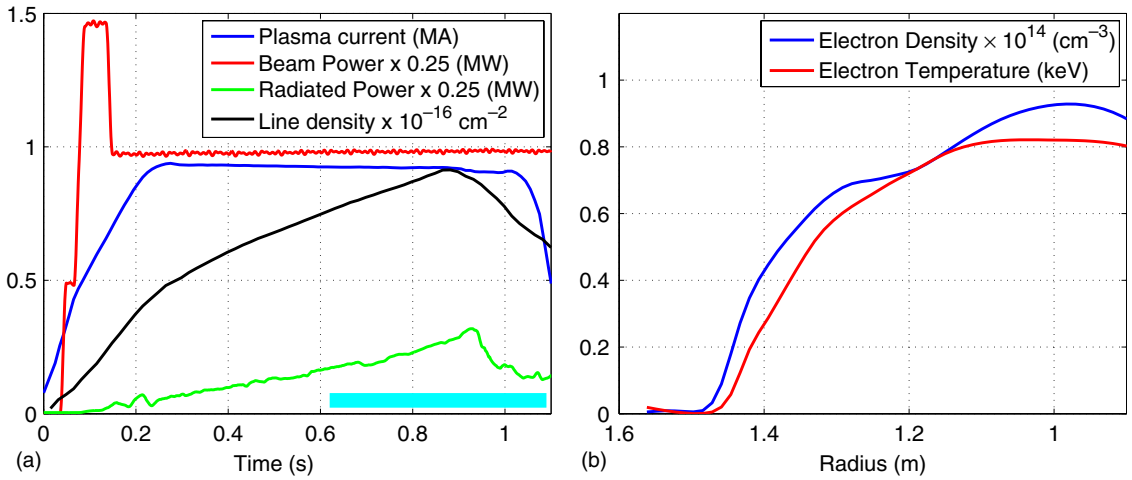

Figure 7. Plasma parameters for the spectrum shown in figure 6. (a) Plasma toroidal current, input power, radiated power and line-averaged electron density as a function of time. The cyan rectangle shows the exposure time of the spectrum. (b) Mid-plane electron density and temperature averaged over the exposure time of the spectrum.

lower than the concentration of fully stripped carbon. This was attributed to low recycling of Li ions from the wall [19].

The emission measured by the TGIS at 135 Å is a blend of charge-exchange emission from C VI $n = 4$–2, electron excited and charge-exchange emission from Li III $n = 2$–1. Figure 11 shows the brightness measured by the TGIS at 135 Å. For comparison, the simulated contribution from the carbon charge exchange is also shown in the figure. The emission cross section for the C VI $n = 4$–2 charge exchange was derived from the ADAS database [15] and the calibration factor derived in section 2.1 was used in comparing with the measured brightness. The comparison confirms that a significant contribution to the brightness of the signal is from Li in the edge of the plasma. However, because of the blend, this direct measurement of the brightness is insufficient to yield quantitative information on Li concentration inside the plasma. Instead one might use the charge-exchange line Li III $n = 3$–1 at 114 Å which is free of any blends. As seen in the figure 8, the intensity of the line is not measurable because of proximity to other charge-exchange lines. However, assuming that the strength of the measured charge-exchange signal is below the noise level of the system yields an upper limit on lithium density inside the plasma: $n(\mathrm{Li}^{3+}) < 0.1 \times n(\mathrm{C}^{6+})$ (emission cross section derived from ADAS database [15]). Better bounds on the low levels of Li concentration are expected from the TGIS upgrade which has an improved spectral resolution of ~6 Å [4].

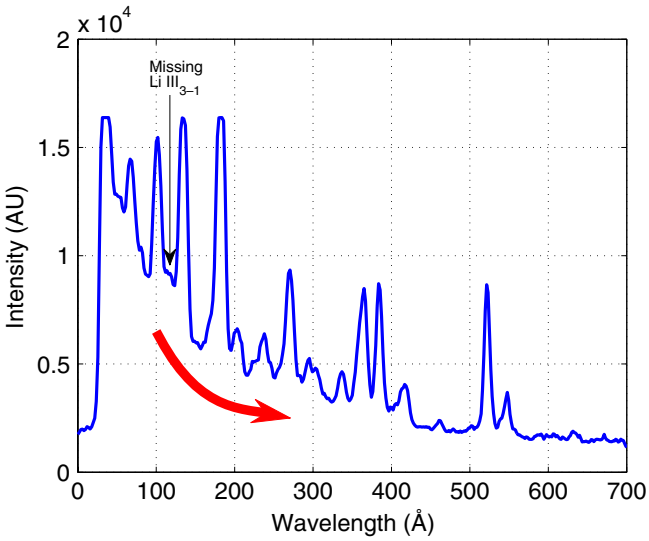

Figure 8. Spectrum observed at tangency radius $R_T = 1.27$ m from figure 6.

Chlorine is the most prominent medium Z impurity in neutral beam heated plasmas on NSTX. Chlorine has been observed in other magnetic fusion experiments in the past [21–23] and its presence is often attributed to it being absorbed during lamination of wall materials [23] or possibly originating from solvent used in cleaning vacuum components [22]. While the source of chlorine in NSTX is not confirmed at this point, its behavior was found to be similar to that on JET tokamak [21], i.e. the level of chlorine reduces gradually after a vessel vent and is not detectable after a few hundred discharges.

The presence of Cl in NSTX was confirmed by the presence of simultaneous emission from Li- and Be-like Cl ions: Cl XIV $2s^2\ {}^1S_0$–$2s2p\ {}^1P_1$, Cl XV $2s\ {}^2S_{1/2}$–$2p\ {}^2P_{1/2,3/2}$ (see figure 12, note that the intensity ratio of the doublet transitions is 1/2). Equilibrium ionization balance calculations show that Cl XIV and Cl XV should exist in the mid-radius region of NSTX plasmas, while Cl XVI should exist from the edge all the way in to the core. As seen from figure 12, the Cl emission is a blend of charge-exchange and electron excitation emission. This makes it difficult to Abel invert the brightness profile. However, approximate density of Cl XVI can be obtained from the charge-exchange contribution in the signal shown in figure 12. If one assumes that the charge-exchange emission cross section for Cl XV 2p–2s is approximately of the same order of magnitude as the charge-exchange emission cross section of Ar XVI $n = 3$–2 [24], one infers an approximate concentration of $n(\mathrm{Cl}^{15+}) \sim 10^{-3} \times n_e$. Also, if one assumes that Li-like and Be-like Cl exist in shells of typical thickness $\delta r \sim 10$ cm, in the mid-radius

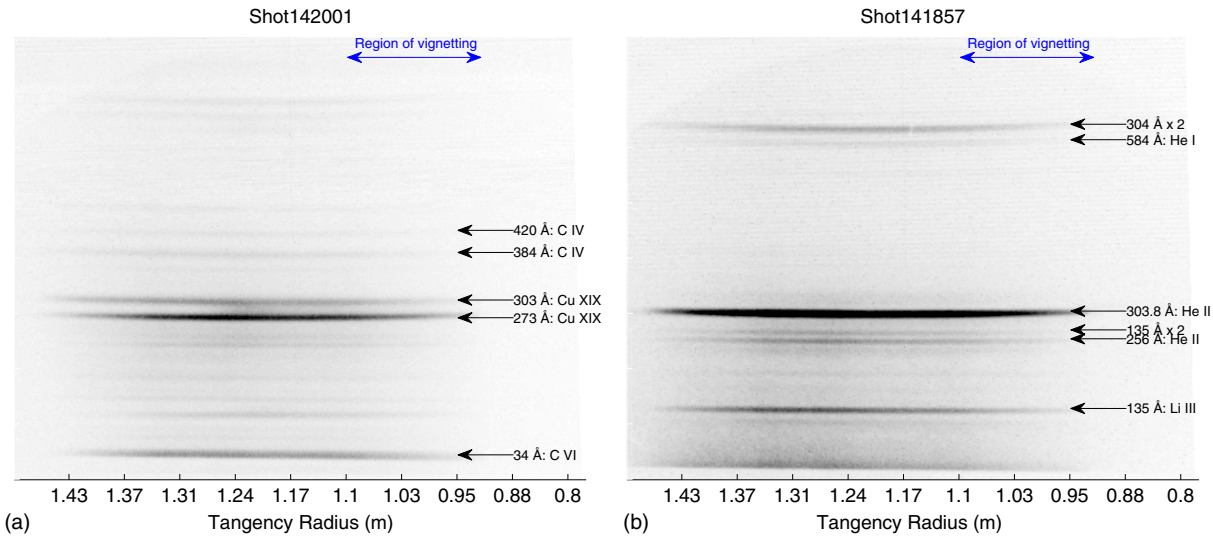

Figure 9. Examples of TGIS spectrum from RF heated shots. (*a*) Spectrum indicating the presence of Cu due to arcing in the antenna in a deuterium shot. (*b*) Spectrum showing the presence of He and Li in a RF heated He plasma.

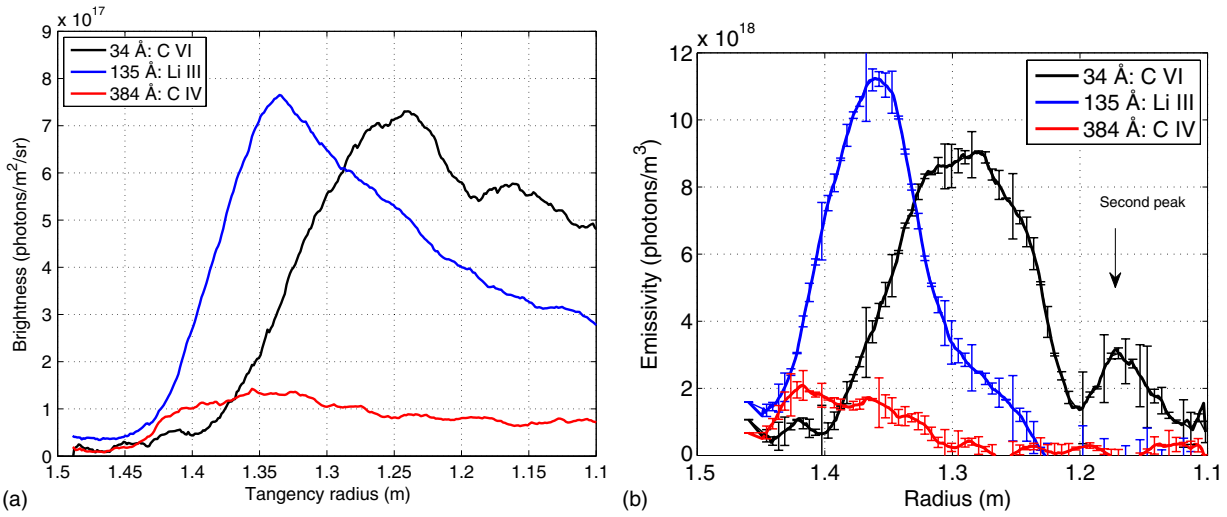

Figure 10. (*a*) Examples of spatial distribution of emission measured in the ohmic plasma shot shown in figure 4. (*b*) Abel inverted radial emissivity and the corresponding error bars from the profiles shown in (*a*).

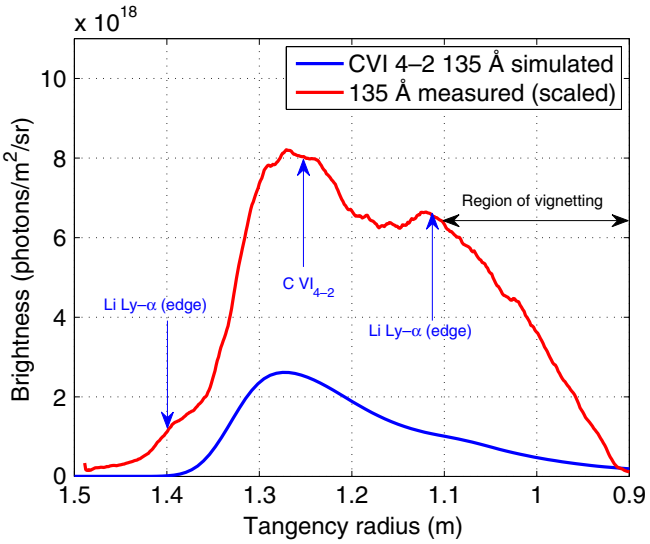

Figure 11. Comparison between measured and simulated charge-exchange C VI $n = 4$–2 line from figure 6.

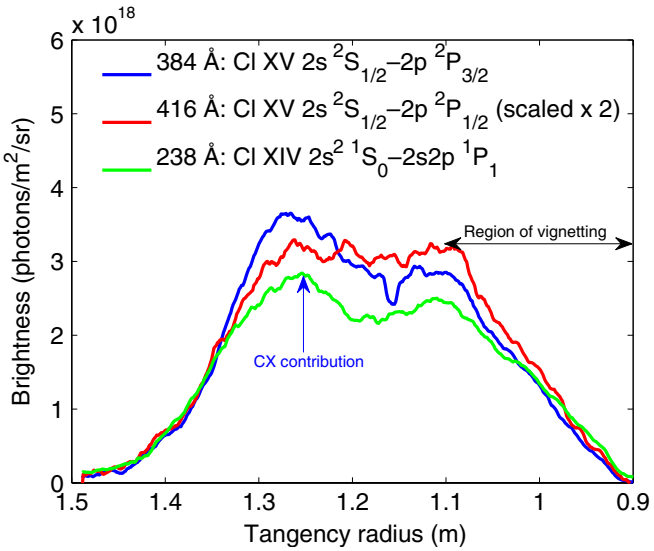

Figure 12. Spatial distribution of Cl emission from spectrum shown in figure 6.

region where the electron temperature is ∼300 eV, one can calculate the expected brightness from their line emission by

$$\text{Brightness} \approx \frac{1}{4\pi}\Delta t f n_e^2 \epsilon(n_e, T_e) 2\delta r, \qquad (4)$$

where Δt is the exposure time of the spectrum, and ϵ is the photon emissivity coefficient derived from ADAS database [15]. An order of magnitude estimate for the Cl density can be found from the above expression: $n(\mathrm{Cl}^{13+}) \sim n(\mathrm{Cl}^{14+}) \sim 5 \times 10^{-5} \times n_e$.

Fe was observed in a few neutral beam heated plasmas, and like Cl, the emission was both from charge exchange and electron excitation. An order of magnitude approximation to the Fe concentration can be found by the method described above: $n(\mathrm{Fe}^{15+}) \sim 5 \times 10^{-6} \times n_e$[3].

[3] As noted in section 2.2, the Cl and Fe concentrations mentioned here are underestimates (but correct order of magnitude) because of the assumed flat response of the detector with increasing wavelength.

5. Conclusion

This paper presented the typical spectra obtained by an imaging XUV spectrometer (TGIS) on NSTX. The space resolving capability of this survey spectrometer was highlighted by the detection of localized charge-exchange radiation (NB heated shots) and also from the electron excited emission from the edge (Abel inverted emissivity from ohmic/RF shots). Furthermore, the spectrometer also detects charge-exchange signals in medium Z impurities (Cl, Fe) and emission from the core during the ramp down phase. For an example of emission peaking in the core during a radiative collapse, the reader is referred to an earlier publication [4].

A fast detection (10 ms) and better resolution (∼6 Å) version TGIS has been implemented successfully [4]. Direct XUV photon detection using CCDs has also been tested in the laboratory [4]. Such upgrades will improve the applicability

of the TGIS for transport experiments, especially involving high Z elements such as tungsten and radiation modeling of the divertor.

Acknowledgments

DK would like to thank Dr Adam Foster and Dr Martin O'Mullane for help with accessing the ADAS atomic database, Dr Jon Menard for suggesting references about Cl in other fusion experiments and the NSTX staff for supporting the operation of TGIS during 2010. DK would also like to thank Dr Deyong Liu (University of California, Irvine) and Dr John Canik (Oak Ridge National Lab) for providing data on halo and recycled neutrals, respectively, to estimate their contribution to the charge-exchange signals. The work at Johns Hopkins University was supported under US DOE Grants Numbers DE-FGO2-86ER53214 and DE-S0000787. The work at PPPL was supported under US DOE Contract Number DE-AC02-09CH11466.

References

[1] Isler R 1984 *Nucl. Fusion* **24** 1599
[2] Dong C, Morita S, Kobayashi M, Goto M, Masuzaki S, Morisaki T and Wang E 2011 *Phys. Plasmas* **18** 082511
[3] Kumar D, Stutman D, Tritz K, Finkenthal M, Tarrio C and Grantham S 2010 *Rev. Sci. Instrum.* **81** 10E507
[4] Kumar D, Stutman D, Bell R E, Finkenthal M, Clayton D J, Tritz K, LeBlanc B P, Diallo A and Podesta M 2011 *38th EPS Conf. Plasma Physics (Strasbourg, France)* P4.047
[5] Wilhein W, Rehbein S, Hambach D, Berglund M, Rymell L and Hertz H M 1999 *Rev. Sci. Instrum.* **70** 1694–9
[6] Kamperschroer J H, Grisham L R, Kokatnur N, Lagin L J, Newman R A, O'Connor T E, Stevenson T N and von Halle A 1995 *Rev. Sci. Instrum.* **66** 130–8
[7] Janev R, Boley C and Post D 1989 *Nucl. Fusion* **29** 2125
[8] Bell R E and Feder R 2010 *Rev. Sci. Instrum.* **81** 10D724
[9] Isler R C 1994 *Plasma Phys. Control. Fusion* **36** 171
[10] von Hellermann M G *et al* 2005 *Phys. Scr.* **T120** 19
[11] Heidbrink W W, Liu D, Luo Y, Ruskov E and Geiger B 2011 *Commun. Comput. Phys.* **10** 716–41
[12] Kowalski M P, Fritz G G, Cruddace R G, Unzicker A E and Swanson N 1986 *Appl. Opt.* **25** 2440–6
[13] Mazzitelli G and Mattioli M 2002 *At. Data Nucl. Data Tables* **82** 313–56
[14] Viezzer E, Ptterich T, Dux R, Kallenbach A and the ASDEX Upgrade Team 2011 *Plasma Phys. Control. Fusion* **53** 035002
[15] Summers H P 2004 *The ADAS User Manual* version 2.6 URL http://www.adas.ac.uk
[16] Mansfield D *et al* 2001 *Nucl. Fusion* **41** 1823
[17] Majeski R, Doerner R, Gray T, Kaita R, Maingi R, Mansfield D, Spaleta J, Soukhanovskii V, Timberlake J and Zakharov L 2006 *Phys. Rev. Lett.* **97** 075002
[18] Bell M G *et al* and the NSTX Research Team 2009 *Plasma Phys. Control. Fusion* **51** 124054
[19] Ono M *et al* 2010 *Proc. 1st Int. Workshop on Lithium Applications for the Boundary Control in Fusion Devices Fusion Eng. Des. (National Institute of Fusion Sciences, Toki, Japan)* **85** 882–9
[20] Podest M, Bell R, Diallo A, LeBlanc B, Scotti F and the NSTX Team 2012 *Nucl. Fusion* **52** 033008
[21] Hedqvist A, O'Mullane M, Nordquist J, Rachlew-Kllne E and Zastrow K D 2000 *J. Phys. B: At. Mol. Opt. Phys.* **33** 375
[22] Rice J E, Marmar E S, Coan T, Allen S L and Cowan R D 1980 *Phys. Rev.* A **22** 310–12
[23] TFR group 1979 *Phys. Lett.* A **73** 13–16
[24] Hung C C, Krstic P and Schultz D State-selective charge transfer cross sections in 15–100 keV/u collisions of Ar^{15-18+} with atomic hydrogen calculated using the CTMC method *Technical Report* Controlled Fusion Atomic Data Center Oak Ridge National Laboratory Oak Ridge, Tennessee 37831-6373, USA http://www-cfadc.phy.ornl.gov/eprints/argon.html